Modeling and Optimization of Axial Winding Segmented Coreless Transformers

Li Lai, Bo Zhang, *Fellow, IEEE*, and Jingyang Lin

***Abstract*—This article presents the modeling and optimization of axial winding segmented coreless transformers (CLTs). By designing the axial segmentation of the winding, the inductance of CLTs is finely achieved, and the optimal electrical, structural, and thermal parameters are obtained accordingly. First, an optimal design methodology of the electrical parameters of the self-sustained CLT is introduced, with the aim of minimizing self-inductance and reducing wire consumption. Second, the inductance model of the proposed CLT is simplified by utilizing the same parameters of the modular segmented unit, and a parameters scanning algorithm with the inductance as the target and the structural parameters as the free degrees is given. Furthermore, a correction factor associated with the radial layers is considered in the ac resistance model of multilayer multisegment CLTs. Combining the loss-thermal iteration model and the system loss model, the structural parameters are optimized, and the output voltage loss is compensated. Finally, a 1.5 kW uniformly sized prototype with a volumetric power density of 13.06 W/cm^3 and a gravimetric power density of 8.57 W/g is fabricated. The prototype achieves a peak efficiency of 96.20% and the maximum temperature and conversion efficiency at maximum output power are 96.8 °C and 93.68%, respectively.**

***Index Terms*—Aerospace power, axial section, coreless transformer (CLT), dc transformer, modeling, optimization.**

I. Introduction

TRANSFORMERS are indispensable devices in electrical energy conversion, which utilize the induction between electricity and magnetism to achieve voltage conversion and electrical isolation [1], [2]. With the development of semiconductors and magnetic materials, magnetic-core transformers (MCTs), represented by ferrite cores, have replaced coreless transformers (CLTs), which utilize air as the magnetic medium, in most applications [3], [4]. Compared with air, soft magnetic materials have a greater magnetic permeability. However, the performance of the MCT is easily affected by factors, such as magnetic saturation, magnetic loss, and temperature. These drastically reduce the reliability of MCTs for applications in harsh environments such as aerospace and deep sea [5], [6]. It means that CLTs with linear magnetization curves still have a great place. In addition, thanks to the application of resonant soft-switching technology, the leakage inductance of loosely coupled CLTs is reused as a resonant inductance, which can significantly reduce the size and number of passive devices and have an advantage in power density [7].

CLTs are widely validated in two typical applications, superconducting transformers [8], [9], [10] and planar coreless transformers [11], [12], [13]. The former does not require much attention to heat dissipation and has almost no conduction loss under ultra-high-current conditions [8]. The latter obtains a very small physical size via MHz frequency, whereas the very low current makes it difficult to increase power [12]. In recent studies [14], [15], [16], CLTs with tens of amperes of currents were validated in terms of electromagnetic, heat dissipation, structural, etc. Compared with MCTs, CLTs can achieve a higher gravimetric power density and similar conversion efficiency. More critically, it can be wound using only conventional Litz wires.

For implementing the two functions of voltage conversion and regulation, two popular design methods were derived for high-frequency MCTs. One method is based on the product of the circuit area and magnetic circuit area [17], and the other is based on the geometrical parameters of the core dimensions [18]. Both methods involve looking up the empirical table to select the core type, and then it is verified by temperature rise. Nevertheless, the influence of multiphysics fields, such as electric, magnetic, and thermal fields, leads to large design deviations. Moreover, relying on experience, optimization is difficult. To overcome these problems, the comprehensive design of transformers for multiobjective optimization [19], [20] and multiphysics analysis [21], [22] have been investigated. These methods can be classified into two types, respectively, finite element simulation (FEA) [21], [22], [23] and analytical model [19], [20], [24]. Although the former is more accurate, it is time-consuming. The latter saves a lot of computational resources and is more compatible with global optimization, so it is more suitable for prevalidation designs.

It is worth pointing out that, the design method of MCTs cannot be referenced by CLTs, and there are significant differences between them in the electromagnetic model, loss model, and thermal model.

1) Electromagnetic model. The relative permeability of Mn–Zn ferrite MCTs ranges from 1000 to 10 000, and its inductance is proportional to the square of turns and inversely proportional to the magnetic resistance. By designing the turns and air gap, the target inductance can be easily

Received 22 May 2024; revised 22 September 2024; accepted 9 November 2024. Date of publication 18 November 2024; date of current version 28 January 2025. This work was supported by the Key Program of National Natural Science Foundation of China under Grant 52130705. Recommended for publication by Associate Editor M. Andersen. *(Corresponding author: Bo Zhang.)*

The authors are with the School of Electric Power, South China University of Technology, Guangzhou 510640, China (e-mail: epbzhang@scut.edu.cn).

Color versions of one or more figures in this article are available at https://doi.org/10.1109/TPEL.2024.3497973.

Digital Object Identifier 10.1109/TPEL.2024.3497973

obtained [17], [18]. However, CLTs with unit relative permeability do not satisfy this simple law, which makes the fine design of the self-inductance and coupling coefficients extremely difficult. Therefore, in [25], the radial offset design of planar transformers is proposed to achieve the target inductance, but it does not apply to wire-wound CLTs. In [26], the axial offset design of wire-wound CLTs is proposed to achieve the target coupling coefficient, and the maximum coupling coefficient is low. Furthermore, due to the low self-inductance and low coupling, a low magnetizing inductance would cause a larger conduction current and turn-off current on the primary side. Overall, the fine parametric electrical design of CLTs with low self-inductance and high coupling is a prerequisite for reducing cost and loss.

2) Loss model. The loss of MCTs includes magnetic loss and copper loss, which can be calculated by the Steinmetz formula [27] and Dowell formula [28], respectively. Differently, the CLT contains only copper loss, and because of the different magnetic field distribution, the one-dimensional Dowell formula does not apply to it. The ac resistance of CLTs includes conduction resistance and induction resistance. The former is related to dc resistance and skin resistance, and the latter is attributed to proximity resistance [29]. Skin resistance is negligible when the strand diameter of the Litz wire is much smaller than the skin depth. In wire-wound CLTs, not only is the proximity effect between the same side winding significant, but also that between the primary and secondary winding, i.e., mutual resistance effect [30]. Papers [29], [30], [31], [32] present several methods for calculating the induction resistance, which is proportional to the square magnetic field of the wire cross-section. The magnetic field can be calculated by the Biot–Savart law [31] or Maxwell equations [32]. However, the accuracy of such methods is much lower in multilayer structures with more inhomogeneous magnetic fields than in single-layer structures [33]. Most importantly, both resistivity and skin depth are temperature-dependent, so loss and temperature affect each other. Besides, the system loss would cause output voltage loss and instability. Hence, a precise loss model of CLTs considering temperature is necessary.

3) Thermal model. The insulation class determines the limit of temperature rise. For example, the Litz wire with temperature level V155 has a maximum operating temperature of 130 °C. However, the average temperature of the core is required to be below 100 °C [14], which limits the ultimate temperature rise of MCTs. Intriguingly, the CLT is not restricted by this limitation, as its winding can be directly cooled and customized. Moreover, the insulation between the winding and core does not need to be considered. In [34], the thermal resistance model of Litz wire provides a more precise prediction of the hotspot, but the difficulty of measuring the thermal resistance between turns and gaps limits its wide application. Thermal empirical formulas are widely used in [35], [36]. Its heat transfer coefficient can be calculated from the surface area and empirical coefficients to quickly predict the average temperature rise. It indicates that the surface area and dimensions of CLTs are also a critical part of the design.

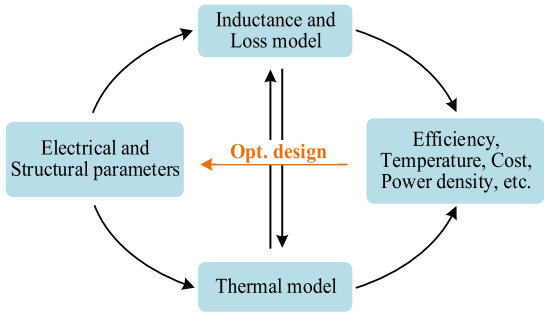

Fig. 1. Associations among analytical models.

In general, it is necessary to consider multiphysics models in the modeling and optimization of CLTs. In [26], the self-sustained *CLLC* CLT utilizing bifurcation is proposed to achieve the same load-independent voltage and current conversion ratios as the ideal transformer, and its efficiency is higher compared with the conventional leakage inductance resonance type CLT [12]. In this article, the modeling and optimization for axial winding segmented CLTs is proposed for the self-sustained transformer. A classic representative of the primary and secondary voltage ratio of 1:1 is employed and it is suitable for dc bus-tie applications [14]. The multimodel correlations are shown in Fig. 1, and the main contributions of this article are as follows.

1) An optimization method for the electrical parameters of self-sustained CLTs is presented with the target of minimizing the self-inductance. The half-load condition is designed at the bifurcation point, from which the analytical equation for the self-inductance is derived. By solving the derivative of the self-inductance with respect to the inductance ratio, then the minimum consumption of Litz wire is achieved.
2) The axial winding segmented design method of coaxial CLT is proposed to achieve the target inductance and optimize the dimensions. Inductance model is simplified by utilizing the consistency parameters of the modular segmented unit. Then, a parameters scanning algorithm with the inductance as the target and internal diameter, number of segments, axial layers, and radial layers as the free degrees is given.
3) A modified ac resistance model and a loss-thermal iterative model for multilayer multisegment CLTs are proposed, and an optimized selection of structural parameters is given. The effect of temperature on resistivity and skin depth is considered and the correction factor is introduced to reduce resistance errors caused by inhomogeneous magnetic fields. Combining the empirical formula of the heat transfer coefficient, a loss-thermal iterative algorithm is established. Then, according to efficiency, temperature rise, power density, cost, and height-outside diameter ratio, the optimal structure parameters are selected.

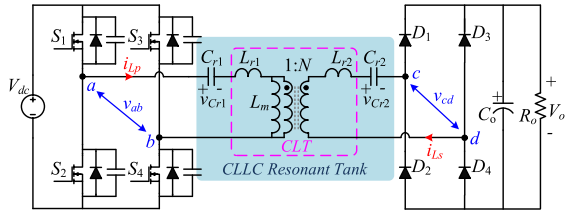

Fig. 2. Circuit topology of the *CLLC* CLT.

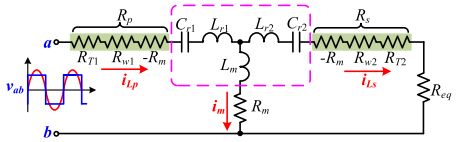

Fig. 3. Lumped circuit of the self-sustained *CLLC* resonant tank at $N = 1$.

Moreover, the output voltage loss from system losses is compensated.

The rest of this article is organized as follows. Section II introduces the optimal design for the electrical parameters of self-sustained CLTs. Section III establishes the fine design for the inductance of the axial multisegment CLT. In Section IV, the loss and thermal are modeled, then parameter selection and output voltage compensation methods are presented. Section V combs the design process in this article. The validation of the prototype is described in Section VI. In Sections VII and VIII, the comparison and extension of this research and the conclusion of this article are given, respectively.

II. Electrical Parameters Optimization of Self-Sustained CLTs

A. Topology Specifications

Fig. 2 shows the circuit topology of the full-bridge *CLLC* CLT. The full-bridge inverter consisting of MOSFETs S_1–S_4 on the primary side converts the dc voltage $V_{\rm dc}$ to ac voltage v_{ab}, and the full-bridge rectifier consisting of diodes D_1–D_4 on the secondary side converts the ac voltage v_{cd} to dc voltage V_o. One difference from conventional converters is that the transformer T is loosely coupled and coreless. More importantly, the inverter adopts self-sustained control, and v_{ab} is in phase with i_{Lp} [12].

For the lumped circuit shown in Fig. 3, the *CLLC* resonant tank is composed of leakage inductance L_{r1} and L_{r2}, magnetizing inductance L_m, and resonance capacitors C_{r1} and C_{r2}. Besides, the inductance ratio is $k = L_m/L_{r1}$, R_o is the load resistance, and C_o is the electrolytic capacitor. It should be emphasized that the conversion ratio N is strictly defined as $N = (L_s/L_p)^{1/2}$ in CLTs, where the primary and secondary self-inductance are $L_p = L_{r1} + L_m$ and $L_s = L_{r1} + N^2 L_m$, respectively.

In this article, the design of self-sustained *CLLC* CLTs with a classical 1:1 voltage conversion is investigated, and its specification parameters are as follows.

1) Maximum output power $P_r = 1500$ W.
2) Input and output voltage $V_{dc} = V_o = 110$ V.
3) Maximum operating frequency $f_{max} = 200$ kHz.

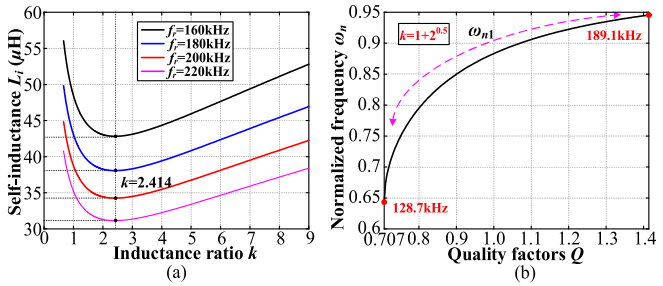

Fig. 4. Working frequency curve. (a) k versus L_i under different f_r. (b) Q versus ω_{n1} at $k = 1 + 2^{0.5}$.

B. Optimization of Electrical Parameters

In the lumped circuit, the ac resistance of CLTs is considered, and the stray capacitor is neglected [30]. R_{w1} and R_{w2} are the ac resistances of the primary and secondary winding, respectively; R_{T1} and R_{T2} are derived from thermal effects; R_m is the mutual resistance; and the load equivalent resistance is $R_{\rm eq} = 8R_o/\pi^2$. Define $R_p = R_{w1} + R_{T1}$, $R_s = R_{w2} + R_{T2}$, and the equivalent resistance of the source $R_n = -v_{ab}/i_{Lp}$. Thus, the impedance matrix $\boldsymbol{Z}$ of the resonant tank can be expressed as follows:

$$\boldsymbol{Z} = \begin{bmatrix} Z_{r1} + Z_m - R_n & -Z_m \\ Z_m & -Z_{r2} - Z_m - R_{\rm eq} \end{bmatrix} \tag{1}$$

where the primary impedance $Z_{r1} = 1/(j\omega C_{r1}) + j\omega L_{r1} + R_p$, the secondary impedance $Z_{r2} = 1/(j\omega C_{r2}) + j\omega L_{r2} + R_s$, and the magnetizing impedance $Z_m = R_m + j\omega L_m$. Define the resonant frequency as $\omega_r = (L_{r1}C_{r1})^{-1/2} = (L_{r2}C_{r2})^{-1/2}$. Hence, the quality factors of the primary and secondary winding are $Q_p = \omega_r L_{r1}/(R_n – R_p)$ and $Q_s = \omega_r L_{r2}/(R_{\rm eq} + R_s)$, respectively.

Neglecting R_m and solving $|\boldsymbol{Z}| = 0$, the normalized bifurcation frequency $\omega_{n1,n2}$ and the quality factor Q_{bp} at the bifurcation point are, respectively

$$\begin{cases} \omega_{n1,n2} = \left(\dfrac{2Q^2(k+1) - 1 \pm \sqrt{4k^2Q^4 - 4kQ^2 + 1 - 4Q^2}}{2Q^2(2k+1)} \right)^{0.5} \\ Q_{bp} = (1 + \sqrt{1+2k})/(2k) < Q \end{cases} \tag{2}$$

where $Q = Q_p = Q_s$, i.e., R_n–$R_p = R_{\rm eq} + R_s$. Because R_n is self-sustained and $R_{\rm eq} >> R_s$, it means that the influence of R_p and R_s on the frequency is small and can be ignored. The operating frequency is limited to ω_{n1} to avoid frequency jitter.

The highest conversion efficiency is achieved at the bifurcation point [26], so the half-load condition is designed at Q_{bp} to achieve high efficiency over a wide load range. Letting $Q = Q_{bp}$ and according to (2), $L_{i=p,s}$ can be expressed as follows:

$$L_i = \frac{16(1+k)V_{\rm dc}^2 Q_{bp}}{\pi^2 \omega_r P_r} = \frac{8(1+k)(1+\sqrt{1+2k})V_{\rm dc}^2}{\pi^2 k \omega_r P_r}. \tag{3}$$

Combining (3) and the specification parameters, the curve of k versus L_i is plotted as shown in Fig. 4(a). As k increases, the curve is a parabola with an upward opening. The derivative of L_i with respect to k is solved as follows:

$$\frac{dL_i}{dk} = \frac{8V_{\rm dc}^2}{\pi^2 \omega_r P_r} \frac{k^2 - \sqrt{2k+1} - k - 1}{k^2\sqrt{2k+1}} \tag{4}$$

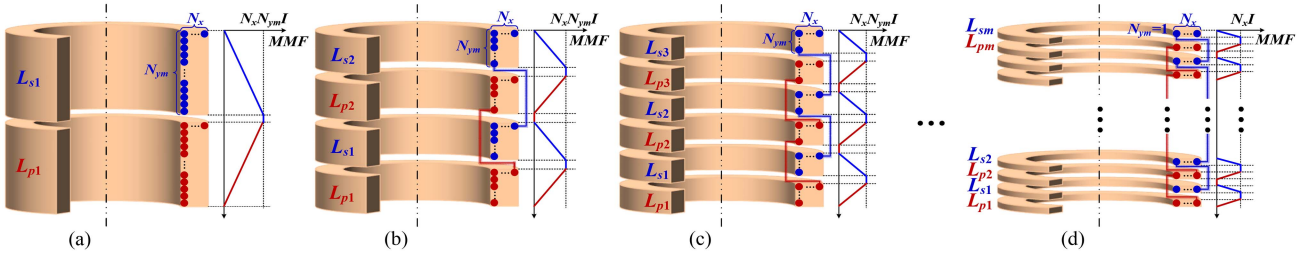

Fig. 5. Axial m-segment layout and MMF distribution. (a) $m = 1$. (b) $m = 2$. (c) $m = 3$. (d) $m = N_y$.

TABLE I
DEVICE SPECIFICATIONS

Device	Parameters
Resonant inductor	L_{r1}=L_{r2}=7.4μH, L_m=17.8μH
Resonant Capacitor	C_{r1}=C_{r2}=86.0nF
Switches (S_1~S_4)	IRFP4227PbF (Si MOSFET)
Doides (D_1~D_4)	MBR40150PT (Schottky Diode)
Digital controller	TMS320F28335
Litz wire	0.05mm×1000strands, Diameter d_r=2.47mm

when $dL_i/dk = 0$, $k = 1 + 2^{0.5}$ and $Q_{bp} = 0.707$ are calculated. Consequently, the minimum L_i can be obtained, which means less wire consumption. Fig. 4(b) shows that the slope and range of ω_{n1} are smaller at $k = 1 + 2^{0.5}$. Because L_i decreases as f_r increases, let $f_r = f_{\max}$. From (2), the maximum switching frequency is $f_{s\_\max} = 189$ kHz $< f_r$.

Because the winding can be cooled directly, the current density J_c is preset to not exceed 9 A/mm^2. The root mean square (RMS) of the winding current is $I_i = 1.11P_r/(\eta V_{\text{in}})$, where η is the system design efficiency. Combining the above analysis, the specifications of the prototype are shown in Table I. A pair of common cathode diodes are connected in parallel to reduce conduction losses.

III. Proposed Axial Multisegment CLTs

The segmentation of the core and winding is employed to design leakage inductance and reduce leakage magnetic losses in MCTs [38]. In this article, the axial winding segmented design is utilized to finely design the self-inductance and inductance ratio and to optimize the dimensions of CLTs. To achieve a homogeneously magnetic field, only segmented designs with symmetrical layouts are considered.

A. Multisegment Structure

Fig. 5 shows the m-segment winding structure and its magnetic motive potential (MMF) distribution. The primary and secondary winding is divided into m-segments, each of which is a unit with the same turns and self-inductance. The radial and axial layers of the unit are N_x and N_{ym}, respectively, and the total axial layers of the CLT are $N_y = mN_{ym}$. Each unit is connected by a wire and has the same MMF increasing from zero to the maximum value $N_{ym}N_xI$. As m increases, the ampere-turns mN_yI of the unit gradually decreases, and so does the leakage magnetic flux, leading to an increase in the coupling coefficient. When $m = N_y$, i.e., $N_{ym} = 1$, the minimum MMF N_xI is realized in Fig. 5(d). When $m = N_y = 1$, the CLT is a planar spiral structure. The advantage of winding segmented structure in CLT applications is that it reduces the maximum MMF, thereby increasing magnetic coupling.

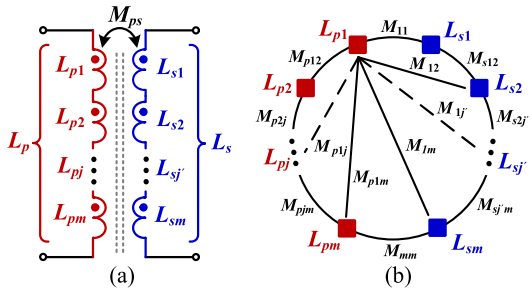

Fig. 6. Equivalent circuit of axial m-segment layout CLTs. (a) Mutual inductance model. (b) Connection of coupled relationships.

Fig. 6(a) shows the equivalent circuit of the proposed CLT. The self-inductance of each unit is L_{ij}, connected in series as L_i, and the mutual inductance between the primary and secondary sides is M_{ps}. Fig. 6(b) presents the coupled relationships of the units, where the mutual inductance between the same-side units is $M_{ijj'}$ and that between the different side units is $M_{jj'}$.

From Fig. 6, according to the circuit superposition theory, the expression of L_i can be written as follows:

$$L_i = \sum_{j=1}^{m} L_{ij} + \sum_{j=1}^{m}\sum_{j'=1}^{m} M'_{ijj}, j \neq j'. \tag{5}$$

Similarly, M_{ps} can be obtained as follows:

$$M_{ps} = \sum_{j=1}^{m}\sum_{j'=1}^{m} M'_{jj}. \tag{6}$$

B. Inductance Model

Fig. 7 shows the cross sections of L_{s1} and L_{pj}. Here, the inner radius, outer radius, and height of the unit are r_{int}, $r_{\text{ext}} = r_{\text{int}} + d_rN_x$, and $h_{ij} = d_rN_{ym}$, respectively, and the Litz wire diameter is d_r. Then, the total height of the CLT is $h = 2mh_{ij}$, and the total turns of L_i is $N_i = mN_xN_{ym}$. It is assumed that the winding is uniformly and tightly wound, and the gap and spiral of the wire are neglected.

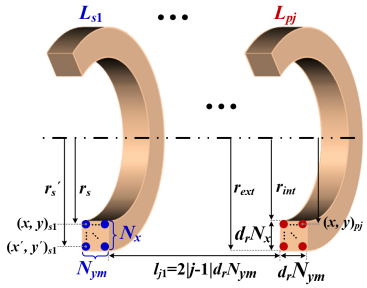

Fig. 7. Cross section of two units.

1) Self-Inductance Calculation of Units: The self-inductance L_1 of a single-turn coil consists of the inductance L_{air} from air magnetic flux and the inductance L_{cu} from conductor magnetic flux. Their formulas are, respectively, [37]

$$L_{\text{air}} = \frac{\mu_0\sqrt{2r_s(2r_s-d_r)}}{\gamma_a}\left[\left(1-\frac{\gamma_a^2}{2}\right)K(\gamma_a)-F(\gamma_a)\right],$$
$$L_{cu} = \frac{\mu_0 r_s}{4}$$
$$L_1 = L_{\text{air}} + L_{cu} = \mu_0 r_s\left(\ln\frac{16r_s}{d_r}-1.75\right),\ 2r_s >> d_r \tag{7}$$

where $\gamma_a = 1–d_r^2/(4r_s–d_r)^2$. L_{ij} can be calculated by the accumulation of L_1 and turn-to-turn mutual inductance. According to Newman formula, L_{ij} can be derived as follows:

$$L_{ij}(N_x, N_{ym}, r_{\text{int}}, d_r) = \sum_{\text{x}=1}^{N_x}\sum_{y=1}^{N_{ym}}\left\{\mu_0 r_s\left(\ln\frac{16r_s}{d_r}-1.75\right)+\mu_0\sum_{\text{x}'=1}^{N_x}\sum_{y'=1}^{N_{ym}}\frac{2\sqrt{r_s'}}{\gamma}\left[\left(1-\frac{\gamma^2}{2}\right)K(\gamma)-F(\gamma)\right]\right\},\quad \text{xy}\neq\text{x}'\text{y}'. \tag{8}$$

In (7) and (8), the vacuum permeability $\mu_0 = 4\pi\times10^{-7}\mu$H/m; the radii of turns $(x,y)_{s1}$ and $(x', y')_{s1}$ are $r_s = r_{\text{int}} + d_r(2x_{s1}–1)/2$ and $r_s' = r_{\text{int}} + d_r(2x_{s1}' - 1)/2$, respectively; $\gamma = (4r_sr_s'/[(r_s + r_s')^2 + d_r^2(y_{s1}–y_{s1}')^2])^{0.5}$; $K(\gamma)$ and $F(\gamma)$ are the first and second complete elliptic integrals, respectively.

2) Mutual-Inductance Calculation of Units: The axial distance between the same-side units is $l_{ijj'} = (2|j–j'|–1)d_rN_{ym}$, and the axial distance between the different side units is $l_{jj'} = 2|j–j'|d_rN_{ym}$. Because of the consistency parameter of the modular segmented unit, the mutual inductance of the units with equal distances shown in Fig. 6(b) are equal, for example, $M_{13} = M_{24}$ and $M_{p15} = M_{s26}$. Therefore, $M_{ijj'}$ and $M_{jj'}$ can be obtained only by calculating the mutual inductance between L_{s1} and other units. Substituting $L_i(2N_{ym})$ and $L_i(N_{ym})$ into (5), M_{11} can be calculated in (9a). Similarly, the expressions of M_{i12}, M_{12}, . . ., M_{i1j}, and M_{1j} are shown in the following:

$$M_{11} = (1/2)[L_{\text{i}}(2N_{ym}) - 2L_i(N_{ym})] \tag{9a}$$
$$M_{i12} = (1/2)[L_i(3N_{ym}) - 3L_i(N_{ym}) - 4M_{11}] \tag{9b}$$
$$M_{12} = (1/2)[L_i(4N_{ym}) - 4L_i(N_{ym}) - 6M_{11} - 4M_{i12}] \tag{9c}$$
$$\cdots$$
$$M_{i1j} = (1/2)[L_i((2j-1)N_{ym}) - (2j-1)L_i(N_{ym})] - \sum_{j'=1}^{j-1}(2j-2j'+2)M_{1j'} - \sum_{j'=2}^{j-1}(2j-2j'+1)M_{i1j'} \tag{9d}$$
$$M_{1j} = (1/2)L_i(2jN_{ym}) - jL_i(N_{ym}) - \sum_{j'=1}^{j-1}(2j-2j'+1)M_{1j'} - \sum_{j'=2}^{j}(2j-2j'+2)M_{i1j'}. \tag{9e}$$

3) Self- and Mutual- Inductance Calculation of CLTs: The above calculation method reduces the calculation number of elliptic integration and increases the calculation speed. Substituting the structural parameters into (8) and (9), M_{i1j} and M_{1j} can be obtained. Furthermore, by combining (5) and (6), L_i and M_{ps} can be calculated. Here, there is $L_m = M_{ps}$.

C. Structural Parameters Sweep

From (5)–(9), it can be seen that r_{int}, m, N_{ym}, and N_x are the free degrees of the design, where N_{ym} is monotonic for L_i. Therefore, assuming the realization of L_i, L_m would increase monotonically with r_{int}. Accordingly, the structural parameter scanning algorithm targeting the inductances L_{i_tar} and L_{m_tar} is proposed, as shown in Fig. 8. In the dotted box, r_{int} and N_{ym} under different m and N_x are calculated iteratively to yield the parameter set $F_{x,m}(r_{\text{int}},N_x,N_{ym},m)$. To prevent calculation overflow, $\Delta r = 0.1$ mm, $m_{\max} = 4$, and $N_{x\_\max} = 4$ are preset.

The distribution of $F_{x,m}$ is shown in Fig. 9. For a given m and N_x, there exists a unique solution for the target inductance.

From Fig. 9(a) and (b), it can be seen that as m and N_x increase, r_{int} decreases significantly. Nevertheless, the height-outside diameter ratio h/r_{ext} increases only with the increase of m, and it is weakly affected by N_x. In other words, winding multisegment design can optimize h/r_{ext} and make CLTs suitable for different dimensional applications.

Fig. 9(c) and (d) give a comparison between the calculated and simulated inductance, with the accuracy of L_i within 3% and L_m within 10%. It should be pointed out that, only considering $N_x \times N_{ym}$ turns, the calculated L_i' would be slightly greater than L_{i_tar}. Therefore, (10) can be employed to correct N_i, and the

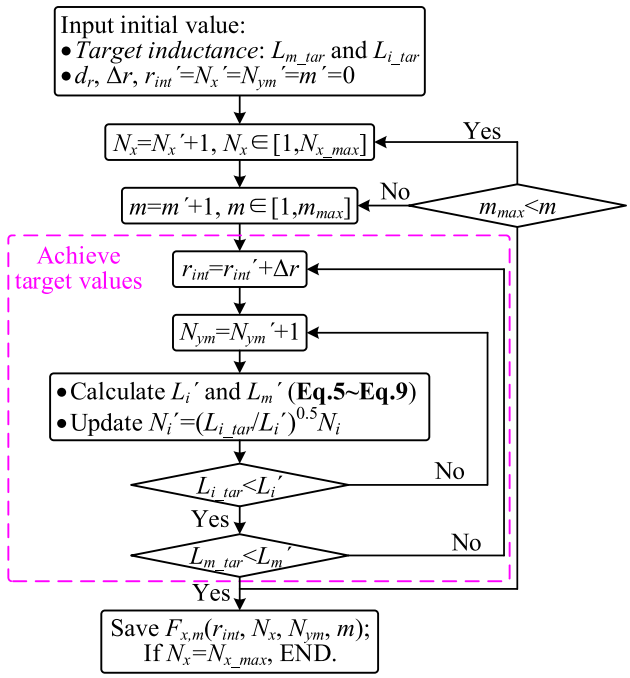

Fig. 8. Structural parameters sweep algorithm.

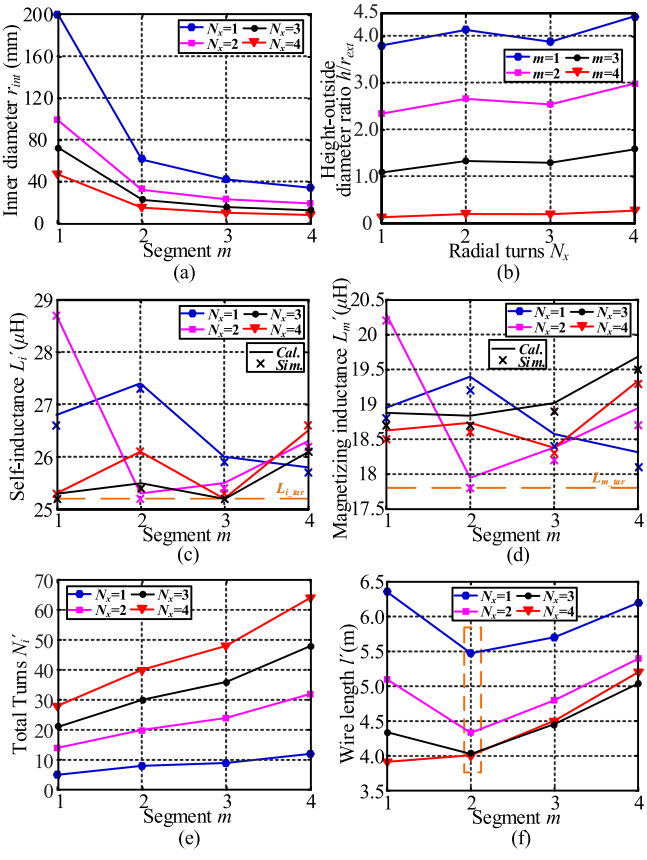

Fig. 9. Distribution of $F_{x,m}$. (a) Inner diameter. (b) Height-outside diameter ratio. (c) Self-inductance. (d) Magnetizing inductance. (e) Total turns. (f) Wire length.

corrected N_i' is shown in Fig. 9(e)

$$N_i' = \lceil \chi m N_x N_{ym} \rceil\,,\ \chi = (L_{i\_\mathrm{tar}}/L_i')^{0.5}. \tag{10}$$

Likewise, the total wire length l' on one-side is corrected and superimposed by each turn as follows:

$$l' = \chi N_y \sum_{x=1}^{N_x} \pi\,[2r_{int} + d_r(2x-1)]. \tag{11}$$

The curve of l' versus m and N_x is shown in Fig. 9(f).

1) Compared with $N_x = 1$, the design with $N_x > 1$ can significantly reduce l' to obtain low cost and lightweight.
2) When $N_x \in [1, 3]$, there is an inflection point at $m = 2$, i.e., there is a minimum l'.
3) When $N_x = 4$, l' monotonically increases with m, and the minimum l' is taken at $m = 1$.

IV. Modeling and Optimization

A. AC Resistance Model

Due to eddy current effects, the ac resistance R_i of CLT is closely related to temperature, frequency, and winding structure, which is critical for verifying system reliability. The losses caused by skin and proximity effects are orthogonal and can be solved separately. The expression for the winding loss P_{un} per unit of length is [32]

$$P_{un} = P_{\mathrm{cond}} + \underbrace{P_{\mathrm{ind\_int}} + P_{\mathrm{ind\_turn}}}_{P_{\mathrm{ind}}} + P_m \tag{12}$$

where P_{cond} is caused by the conduction resistance R_{un_cond}; P_{ind} is caused by the strand-strand inductive resistance $R_{un\_\mathrm{ind\_int}}$ and the turn-turn inductive resistance $R_{un\_\mathrm{ind\_turn}}$ on same-side winding; and P_m is caused by the turn-turn inductive mutual resistance R_{un_m} at the different side. Corresponding to Fig. 3, there is $R_w + R_T = R_{\mathrm{cond}} + R_{\mathrm{ind\_int}} + R_{\mathrm{ind\_turn}}$.

The ideal Litz wire consists of n_{litz} strands, and the current is evenly distributed across each strand. Here, the temperature rise $\Delta T = T–T_o$ is considered. From ΔT and f_s, the skin depth δ can be expressed as follows:

$$\delta(T) = \left(\frac{\rho_{cu}(T)}{\pi\mu_0\mu_r f_s}\right)^{0.5} = \left(\frac{\rho_{cu}(T_o)\,[1+\tau\Delta T]}{\pi\mu_0\mu_r f_s}\right)^{0.5} \tag{13}$$

where the relative permeability of copper is $\mu_r = 1$; the temperature coefficient is $\tau = 3.81 \times 10^{-3}$/°C; the resistivity is $\rho_{cu}(T_o) = 17.24 \times 10^{-9}$ Ω·m at the normal temperature $T_o = 20$ °C.

The conductor penetration rate ζ is defined as follows:

$$\zeta = \sqrt{\pi} d_z/(2\delta(T)) \tag{14}$$

where d_z is the diameter of a single strand.

Satisfying $\zeta \le 2$, the conduction resistance R_{un_cond} is

$$R_{un\_\mathrm{cond}} = \frac{2\zeta\rho_{cu}}{\pi n_{\mathrm{litz}} d_z^2}\frac{\sinh\zeta + \sin\zeta}{\cosh\zeta - \cos\zeta} \approx \frac{\rho_{cu}}{\pi n_{litz} d_z^2}\left(4 + \frac{\zeta^4}{30}\right). \tag{15}$$

Because d_z is small enough, the skin effect is neglected and R_{un_cond} is equal to the dc resistance.

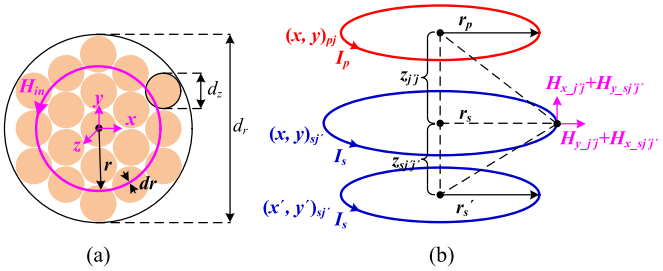

Fig. 10. Distribution of the magnetic field. (a) Magnetic field on the cross section of Litz wire. (b) External magnetic field across Litz wires.

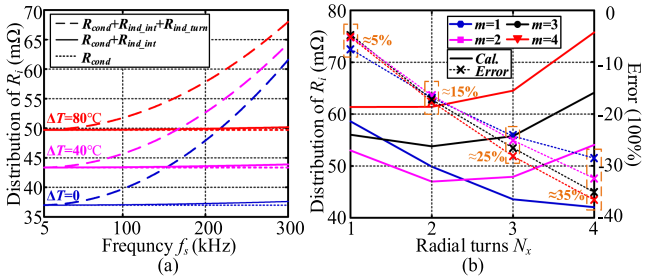

Fig. 11. Distribution of R_i. (a) R_i versus f_s and ΔT at $N_x = 3$ and $m = 2$. (b) Calculations are compared with simulations at $\Delta T = 0$ and $f_s = 200$ kHz.

The inductive resistance per unit of length on the same side winding, R_{un_ind}, can be expressed as follows:

$$R_{un\_\mathrm{ind}} = \frac{1}{2} n_{\mathrm{litz}} \zeta \rho_{cu} H_{\mathrm{ind}}^2 \frac{\sinh\zeta - \sin\zeta}{\cosh\zeta + \cos\zeta} \approx \frac{n_{\mathrm{litz}} \rho_{cu} \zeta^4 H_{\mathrm{ind}}^2}{12} \tag{16}$$

where H_{ind}^2 is the average of the square field on the wire cross section created by a current with amplitude $I = 1$ A. It includes two parts, H_{in} and H_{ext}, with $H_{\mathrm{ind}}^2 = H_{\mathrm{in}}^2 + H_{\mathrm{ext}}^2$. The former is induced by the strand-strand magnetic field, while the latter is caused by the turn-turn magnetic field on the same side.

Due to the low frequency, the time-varying magnetic field can be regarded as a quasi-stationary field. Fig. 10 shows the distribution of the magnetic field, where $r_p = r_{\mathrm{int}} + d_r(2x_{pj}–1)/2$, $z_{j'j} = d_r(y_{pj} + N_{ym}–y_{sj'}) + l_{jj'}$, and $z_{sj'j'} = d_r(y_{sj'}–y_{sj'}')$. According to Fig. 10(a), H_{in}^2 can be calculated by Ampere Law as follows:

$$H_{\mathrm{in}}^2 = \frac{2}{\pi d_r} \int_0^{\frac{d_r}{2}} \left(\frac{I}{2\pi r} \cdot \frac{4r^2}{d_r^2} \right)^2 dr = \frac{I^2}{3\pi^2 d_r^2}. \tag{17}$$

Substituting (17) into (16) yields $R_{un\_\mathrm{ind\_int}}$.

As shown in Fig. 10(b), the current in the Litz wire is regarded as a filamentary current concentrated at the centre of the cross-section, and its magnetic field H_{ext} is created by the rest of the turns. Because of the $2r_i >> d_r$ and the symmetry of the circular winding, $H_{sj'j'}$ generated by 1A-turn $(x, y)_{sj'}$ at turn $(x', y')_{sj'}$ can be calculated by superposing the vector fields in the x- and y- directions. Here, the currents of the other turns are set to 0. According to the Biot–Savart Law [31], ${H_{sj'j'}}^2$ is calculated as follows:

$$\begin{cases} {H_{sj'j'}}^2 = H_{x\_sj'j'}^2 + H_{y\_sj'j'}^2 \\ H_{x\_sj'j'} = \frac{I}{4r_s'} \frac{\gamma}{\pi\sqrt{\alpha}} \left[\frac{1-\alpha^2-\beta^2}{4\alpha(1-\gamma^2)} \gamma^2 F(\gamma) + K(\gamma) \right] \\ H_{y\_sj'j'} = \frac{I}{4r_s'} \frac{\lambda\gamma}{\pi\sqrt{\alpha}} \left[\frac{1+\alpha^2+\beta^2}{4\alpha(1-\gamma^2)} \gamma^2 F(\gamma) - K(\gamma) \right] \end{cases} \tag{18}$$

where the parameters are defined as $\alpha = r_s/r_s'$, $\beta = z_{sj'j}/r_s'$, and $\lambda = z_{sj'j}/r_s$, respectively. According to the superposition theory of electromagnetic field, H_{ext}^2 on a single turn can be calculated by accumulating the magnetic fields generated by other turns on the same side, which is represented as follows:

$$H_{ext}^2 = \left[\sum_{x\prime=1}^{N_x} \sum_{y'=1}^{N_y} (H_{x\_sjj'}) \right]^2 + \left[\sum_{x\prime=1}^{N_x} \sum_{y'=1}^{N_y} (H_{y\_sjj'}) \right]^2,$$

$$xy \neq x'y'. \tag{19}$$

Substituting (19) into (16) yields the turn-to-turn inductive resistance $R_{un\_\mathrm{ind\_turn}}$ of turn $(x,y)_{sj'}$.

Similarly, the accumulated magnetic field H_m generated by all turns of the different side winding on turn $(x, y)_{sj'}$ can be obtained, and the mutual resistance per unit of length R_{un_m} is

$$R_{un\_m} = \frac{P_m}{I_{Lp} I_{Ls} \cos\theta_{ps}} = \frac{1}{12} n_{\mathrm{litz}} \rho_{cu} \zeta^4 |H_{\mathrm{ext}}| \cdot |H_m| \tag{20}$$

where the current phase between the primary and secondary sides is $\theta_{ps} = \angle[(Z_{r2} + Z_m)/Z_m]$.

According to (11)–(20), the total ac loss P_T of the CLT is derived by accumulating P_{un} on the primary and secondary turns, which is expressed as follows:

$$\begin{aligned} P_T = 2\chi I_{Lp} I_{Ls} \sum_{\mathrm{x}=1}^{N_x} \sum_{y=1}^{N_y} \pi \left(2r_{\mathrm{int}} + d_r(2x-1)\right) \\ \cdot \left[\left(\frac{\rho_{cu}(T)}{\pi n_{\mathrm{litz}} d_z^2} \left(4 + \frac{\zeta^4}{30} \right) + \frac{1}{12} n_{\mathrm{litz}} \rho_{cu} \zeta^4 \right. \right. \\ \left. \left. \times \left({H_{\mathrm{in}}}^2 + {H_{\mathrm{ext}}}^2 + |H_{\mathrm{ext}}| \cdot |H_m| \cos\theta_{ps} \right) \right] \right. \end{aligned} \tag{21}$$

At the maximum power, there is $\theta_{ps} = 162°$, i.e., $\cos\theta_{ps} \approx -1$, which indicates that P_m diminishes the loss. It is important to point out that the neglect of P_m is more conservative for the system design. Here, P_m is ignored in this article.

Fig. 11(a) illustrates the curve of R_i versus f_s and ΔT at $N_x = 3$ and $m = 2$.

1) Within 200 kHz, $R_{\mathrm{ind\_int}}$ can be ignored. Besides, R_{cond} and $R_{\mathrm{ind\_int}}$ are both independent of the winding structure, which can be reduced by increasing the cross-sectional area $n_{\mathrm{litz}} {d_z}^2/4$ of the Litz wire.
2) Although R_{cond} is weakly affected by frequency, it is positively correlated with temperature. In contrast, since an increase in temperature leads to an increase in ζ, a smaller $R_{\mathrm{ind\_turn}}$ can be realized.
3) because of $\omega_{n1} < 1$, the self-sustained CLT has smaller ac resistance, resulting in lower loss and temperature rise compared with leakage inductance resonant CLTs [17].

Fig. 11(b) depicts the comparison between FEA simulation and analytical calculation of R_i at $\Delta T = 0$ and $f_s = 200$ kHz. The increase of N_x results in nonideal inhomogeneous distribution of

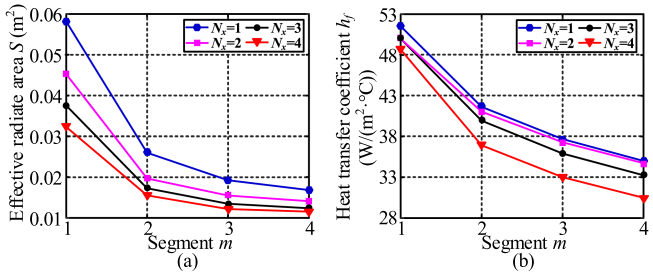

Fig. 12. Distribution of S and h_f. (a) Effective heat-transfer area. (b) Heat transfer coefficient.

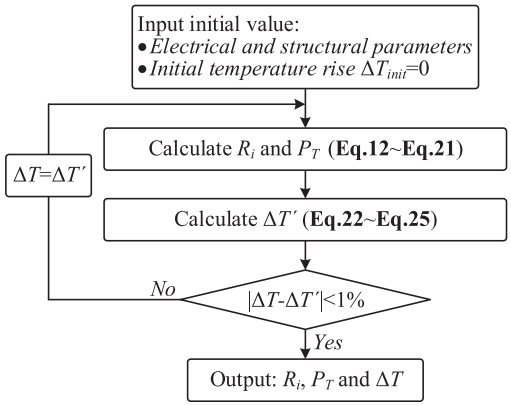

Fig. 13. Loss-thermal iterative calculation.

magnetic field and current [33], which increases the calculation error with Error $\approx$ 0.95–(N_x–1)10%. A convenient way for compensating the error is to introduce a correction factor [36], with $R_i' = R_i/[0.95–(N_x–1)10\%]$, and the error is only within the acceptable 3% after compensation. Besides, in three dimensions, the twisting factor also should be considered.

B. Thermal Model

In fact, the thermal and loss of CLTs not only affect each other, but are also closely related to the electrical and structural design. For quick verification, only the average temperature rise of the CLT is analyzed. As the hotspot near the winding center is 10–20 °C higher than the surface temperature [24], the margin is considered. It is designed as $\Delta T_{\max} = 90$ °C, i.e., the maximum operating temperature is $T_{\max} = 110$ °C, which is lower than the maximum allowable temperature of 130 °C [14]. Compared with natural cooling (1–10 W/(m^2·°C)), the heat transfer coefficient of forced air cooling can reach 10–100 W/(m^2·°C), and it is widely used in kW-class power electronic equipment. As shown in Fig. 17(c), the thermal loss of the prototype is mainly exchanged by convection between the surface and air. Because of $h > r_{\text{est}}–r_{\text{int}}$, the air cooling direction is parallel to the axis to increase the heat-transfer area and reduce turbulence. Neglecting the bottom area, the effective heat-transfer area S is [35]

$$S = 2\pi d_r m N_{ym}(r_{\text{int}} + r_{\text{ext}}) + \pi(r_{\text{ext}}^2 - r_{\text{int}}^2). \tag{22}$$

TABLE II
SPECIFICATION OF PROTOTYPE

Device	Variable	Parameters
CLT	Inner diameter r_{int}	23 mm
	Radial layers N_x	3
	Axial layers of unit N_{ym}	4
	Segments m	2
	Gravimetric power density	8.57 W/g
	Volumetric power density	13.06 W/cm^3
	Toll Wire length	Pri. 4.0m; Sec. 4.34 m
Cooling Fan	Dimension	80×80×25 mm^3
	Max Airflow Q_f	0.0215m^3/s
	Maximum Power	4.5 W

According to engineering experience, the air volume Q_f of the cooling fan needs to satisfy

$$Q_f \approx (1.5–2) \times P_T/(C_{\text{air}}\rho_{\text{air}}\Delta T_{\text{air}}) \tag{23}$$

where the air-specific heat capacity is $C_{\text{air}} = 1005$ J/(kg·°C), the air density $\rho_{\text{air}} = 1.23$ kg/m^3, and the temperature difference between the air outlet and air inlet is $\Delta T_{\text{air}} < 5$ °C.

Here, the heat transfer coefficient h_f is predicted as [36]

$$h_f = (3.33 + 4.8v^{0.8})/l_c^{0.288} \tag{24}$$

where v is the velocity of the approaching flow, defined as $v =$ 4 m/s; the characteristic length is $l_c = 2mh_{ij} + d_rN_x$. From the above parameters, the specification of the cooling fan can be selected as shown in Table II.

According to Newton cooling formula, without considering radiation, the winding temperature rise ΔT is expressed as follows:

$$\Delta T = P_T/(Sh_f). \tag{25}$$

From (25), S and h_f, which are related to the structural parameters, directly affect ΔT. Combining the parameters in Fig. 9, the distributions of S and h_f, are plotted as shown in Fig. 12(a) and (b). As m and N_x increase, both S and h_f decrease, indicating that heat dissipation capacity becomes weaker.

Analyzing (13), (21), and (25), it is clear that ΔT and δ affect each other, and the temperature-dependent parameters are accurately predicted by iterative calculations. Fig. 13 shows the loss-thermal iterative calculation process. With electrical and structural parameters, and initial temperature rise $\Delta T_{\text{init}} = 0$ as input, the calculation is completed when the error between the current value and the previous one is less than 1%, otherwise, ΔT is returned and the operation continues.

C. Optimization of Structural Parameters

The temperature rise is a given restrictive condition, besides that, efficiency, cost, height-outside diameter ratio, volumetric power density (VPD), and gravimetric power density (GPD) are also key items for evaluating system performance. These items are shown in Fig. 14, where the twisting factor of the Litz wire is considered. The detailed analysis is as follows.

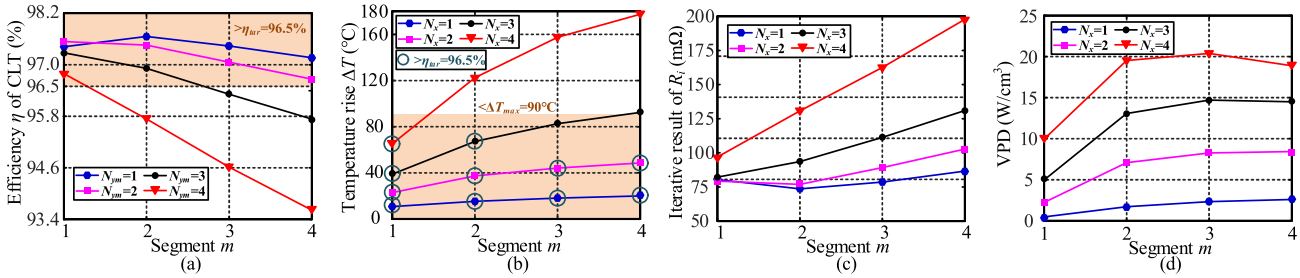

Fig. 14. Evaluation items. (a) Efficiency of CLT. (b) Temperature rise. (c) AC resistance. (d) Volumetric power density.

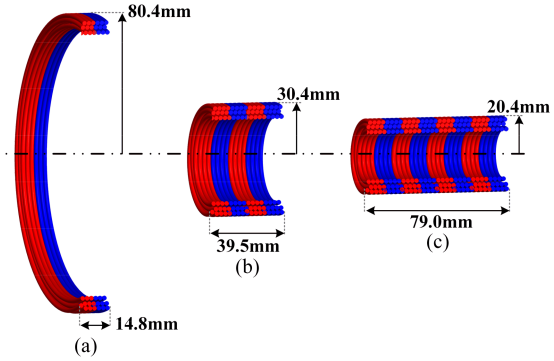

Fig. 15. Height-Outside diameter ratio for different m when $N_x = 3$. (a) $m = 1$, $h/r_{\text{ext}} = 0.18$, and VPD=4.98 W/cm^3. (b) $m = 2$, $h/r_{\text{ext}} = 1.30$, and VPD=13.06 W/cm^3. (c) $m = 4$, $h/r_{\text{ext}} = 3.87$, and VPD=14.5 W/cm^3.

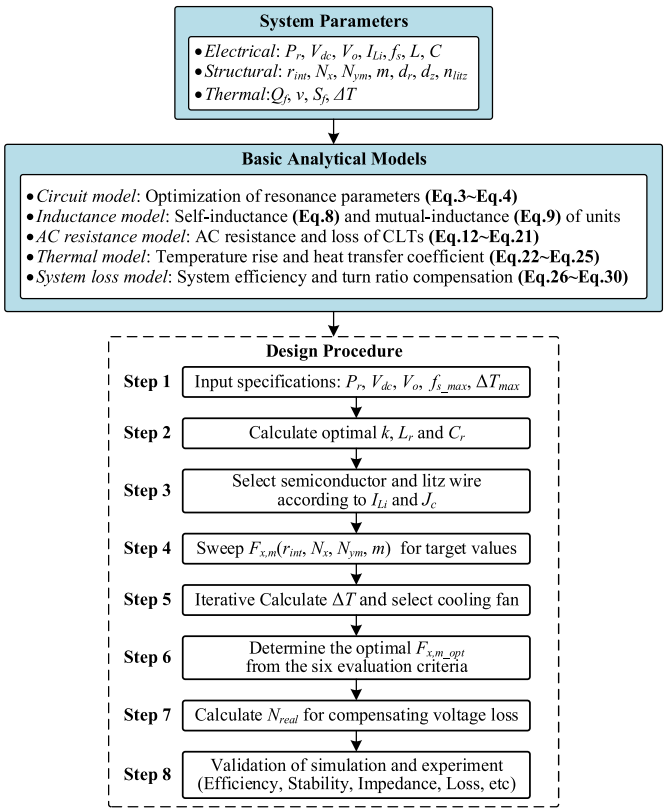

Fig. 16. Design process based on multianalytical models.

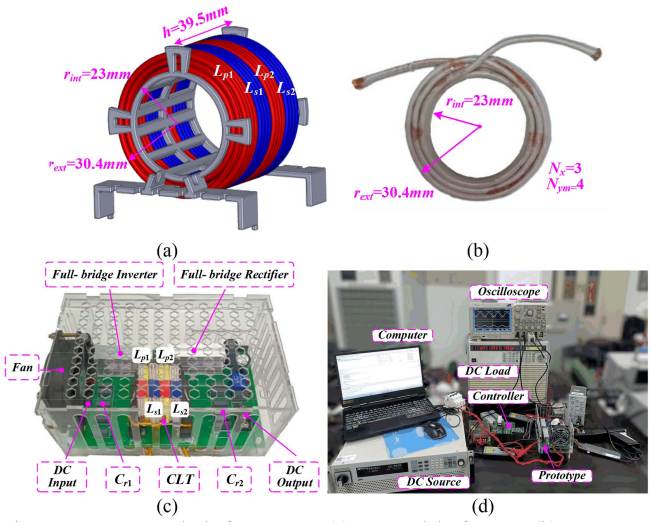

Fig. 17. Prototype and platform setup. (a) 3-D model of CLTs. (b) Segmented unit. (c) Experimental prototype. (d) Experimental platform.

1) Efficiency, ΔT, and VPD: According to the loss-thermal iterative algorithm, the efficiency, ΔT, and R_i under different structural parameters are calculated. Fig. 14(a) shows that the increases in both m and N_x result in a decrease in efficiency and an increase in ΔT. The fact is that both S and h_f decrease, leading to an increase in R_i. The system efficiency at the maximum output power is designed to be 93.0%, so the target efficiency of CLT is set as $\eta_{\text{tar}} = 96.5\%$. The parameters are filtered utilizing $\Delta T_{max} = 90$ °C and $\eta_{\text{tar}} = 96.5\%$ as shown by the circles in the orange part of Fig. 14(a) and (b).

The volume of the CLT is $V = \pi h r_{\text{ext}}{}^2$ and VPD is shown in Fig. 14(d). When $N_x = 1$, it has a smaller VPD but the heat-transfer area is larger, which satisfies the thermal requirements even with natural cooling. It is highlighted that when $N_x = 4$, it has a larger VPD but lower efficiency. Even more, the more layers there are, the more significant the temperature gradient distribution is and the higher the hotspot is. Therefore, the case of $N_x < 4$ is considered in the design.

2) Cost and GPD: Ignoring the bobbin, the cost and GPD of the CLT are proportional to the wire length l. In the electrical parameter design, the minimum self-inductance is designed to

obtain a smaller l. From Fig. 9(f), it can be seen that the minimum l is realized at $m = 2$.

3) Height-Outside Diameter Ratio: h/r_{ext} is determined by the structural parameters of different dimensional applications, which affects the heat dissipation capacity. At $m = 1$ and $m = 4$, the dimensions of the CLT are flat and long cylinders, respectively, as shown in Fig. 15. By designing h/r_{ext} in the range [1], [3], the dimensions are more uniform and similar to that of MCTs. Moreover, r_{ext} should be slightly smaller than the radius of the cooling fan to improve space utilization.

From $m = 2$, $h/r_{\text{ext}} \in [1,3]$, $N_x < 4$, $\eta_{\text{tar}} = 96.5\%$, and $\Delta T_{\max} = 90$ °C, two sets of $F_{x,m}$ can be obtained, with $N_x = 2$ and $N_x = 3$, respectively. Because of the higher VPD and smaller l, the design with $N_x = 3$ is chosen. The detailed specification parameters of the optimal set F_{x,m_opt} are shown in Table II. In fact, multilayer multisegment structures would lead to difficulties in fabrication, so their number is small enough that a complex optimization algorithm is not required in this article.

D. Compensation of Output Voltage Loss

The loss of power and output voltage caused by nonideal factors is inevitable, so it is necessary to analyze the system loss and compensate for output voltage loss. The system loss is modeled and its total loss P_{tot} includes MOSFETs loss P_s, rectifier diode loss P_D, resonant capacitor loss P_C, and winding loss P_T (see (21)). Thus, P_{tot} is

$$P_{\text{tot}} = P_s + P_D + P_C + P_T. \tag{26}$$

P_s, P_D, and P_C are analyzed in detail as in (27)–(29).

1) MOSFETs Loss P_s: Because of zero-voltage turn-ON, the turn-ON loss is not considered, and P_s contains only the conduction loss P_{s_con} and the turn-OFF loss P_{s_off}, as follows:

$$\begin{aligned} P_s &= P_{s\_\text{con}} + P_{s\_\text{off}} \\ &= \frac{V_{\text{dc}} I_{Lp}}{V_n I_n} \left[2 I_{Lp}^2 R_{ds}(T_j, V_n, I_n) + 4 f_s E_{\text{off}}(T_j, V_n, I_n) \right] \end{aligned} \tag{27}$$

where R_{ds} is the ON-resistance; E_{off} is the turn-OFF loss; T_j is the junction temperature; V_n is the test voltage; and I_n is the test current. These parameters are given in the datasheet.

2) Rectifier Diode Loss P_{D}: Diodes do not have reverse recovery and only the conduction loss is calculated as follows:

$$P_D = \frac{V_o I_{Ls}}{V_n I_n} \frac{4\sqrt{2}}{\pi} I_{Ls} V_F(T_j, V_n, I_n) \tag{28}$$

where V_F is the diode forward voltage.

3) Resonant Capacitor Loss P_{C}: The loss tangent of resonant capacitor is δ, and P_C is written as follows:

$$P_C = (I_{Lp}^2/C_{r1} + I_{Ls}^2/C_{r2}) \tan\delta/(2\pi f_s). \tag{29}$$

Compared with conventional leakage inductance resonant CLTs, self-sustained CLTs achieve the maximum equivalent magnetizing inductance and $\omega_n < 1$, resulting in smaller ac resistance, primary RMS current, and MOSFET turn-off current. Consequently, P_{tot} is also smaller.

The system efficiency is $\eta = P_r/(P_r + P_{\text{tot}}) \times 100\%$. Considering the effect of nonlinear terms such as dead zones, the practical voltage gain is $G_{\text{real}} < \eta N$. It follows that the practical turns ratio N_{real} needs to satisfy

$$N_{\text{real}} > G/\eta. \tag{30}$$

The turns on the secondary side are added to compensate for the output voltage loss, while a slight increase in mutual inductance does not affect the stability of the system.

V. Design Procedure

The design parameters include electrical, structural, and thermal parameters that interact with each other. According to the multi-analytical models of circuit, inductance, ac resistance, thermal, and system loss, this section combs the process of the proposed design methodology. Fig. 16 shows the design procedure in this article.

First, the specification parameters of the system are given, such as power, voltage, and frequency. Consequently, the electrical parameters are optimized independently to reduce the coupling of the models (Steps 1–3). The optimal k achieving the minimum inductance is derived from which the resonance parameters are calculated. Considering that the winding is directly air-cooled, J_c of CLTs can be greater than that of MCTs.

Second, with L_i and L_m as the target inductance, the structural parameter set $F_{x,m}(r_{\text{int}}, N_x, N_{ym}, m)$ satisfying the requirements are scanned, and the loss and ΔT are iteratively calculated (Steps 4–6). The six items of efficiency, cost, height-outside diameter ratio, VPD, and GPD are used to evaluate the optimal F_{x,m_opt}. Combined with the loss of CLTs, the system efficiency is calculated to obtain N_{real} (Step 7). The dimensions of the designed CLT are more uniform and similar to that of MCTs.

Finally, the performances of the proposed design, such as loss, temperature rise, and output voltage stability, are verified in simulation and experiment. It is worth pointing out that if the design fails to meet the thermal requirements, it can be avoided by lowering J_c or enhancing the cooling air.

VI. Experimental Prototype and Verification

A. Prototype Fabrication

As shown in the 3-D model in Fig. 17(a) and the segmented unit in Fig. 17(b), there is a uniform dimension with $h/r_{\text{ext}} = 1.3$. The proposed CLT can be assembled from four units, and the unit can be manufactured modular at a lower cost. The prototype is shown in Fig. 17(c) and its parameters are shown in Tables I and II.

The bobbin of the CLT is three-dimensional printed using polyamide-12 with a maximum operating temperature of 175 °C, avoiding the risk of overheating. Moreover, in order to enhance the ability of heat dissipation in the inner conductor, the bobbin is designed in a hollow shape. The prototype shell is not in direct contact with the heat source, thus acrylic with a maximum working temperature of 80 °C is employed, which is manufactured by CNC and slotted to ensure airflow. The radius of the cooling fan is slightly larger than r_{ext}, at 40 mm. Referring to the magnetic

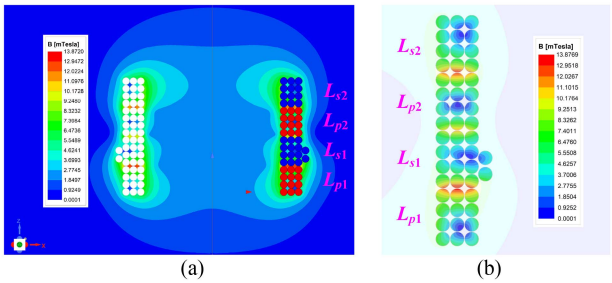

Fig. 18. Distribution of Magnetic field. (a) External magnetic field. (b) Magnetic field in wire cross-section.

TABLE III
CALCULATED, SIMULATED AND MEASURED PARAMETERS

Var. (N_{real}=1.08)	Cal.	2D-Sim.	Meas.	Err.(%)
Self- and Mutual- Inductance				
Pri. L_p	25.20μH	25.41μH	24.30μH	0.83/3.70
Sec. L_s	29.39μH	30.05μH	28.47μH	2.20/3.23
Mut. M_{ps}	17.80μH	19.70μH	18.41μH	9.64/3.31
Self- and Mutual- resistance				
Pri. R_p	63.89mΩ	63.84mΩ	82.20mΩ	0.078/22.27
Sec. R_s	74.52mΩ	74.28mΩ	96.89mΩ	0.32/23.09
Mut. R_m	7.90mΩ	9.60mΩ	7.10mΩ	17.71/11.27

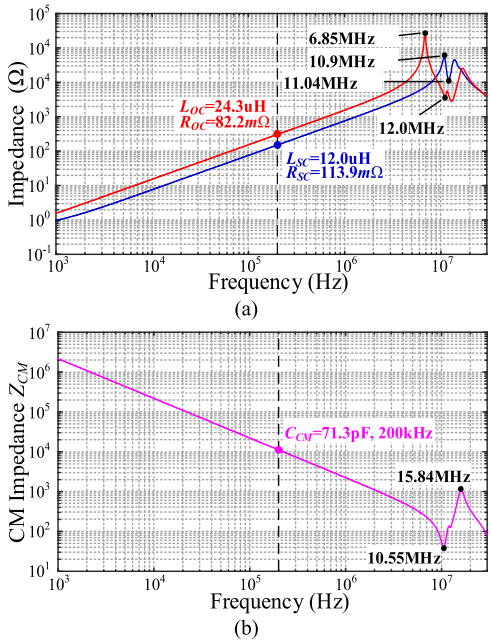

Fig. 19. Measured impedance. (a) Open-circuit $Z_{\rm OC}$ and short-circuit impedance $Z_{\rm SC}$. (b) Common-mode impedance $Z_{\rm CM}$.

field distribution, its distance from the CLT is 40 mm to avoid eddy current effects.

The test platform is shown in Fig. 17(d), and the laboratory equipment includes dc power supply IT6006C, electronic load Chroma 63204, voltage probe Cybertek P1300, current probe Cybertek CP305, and oscilloscope Tektronix DPO3014.

Fig. 18(a) shows the external magnetic field distribution of the CLT. Two turns are added on the secondary side to compensate for the output voltage loss. There is a minimum magnetic field between L_{p2} and L_{s1}, and the maximum magnetic field is located between L_{p1} and L_{s1}. These distributions are consistent with the analysis in Fig. 5(b). Fig. 18(b) shows the magnetic field in the wire cross section. The inhomogeneous distribution of the magnetic field leads to the inhomogeneous distribution of the current, which is the reason for the calculation error of (21). The maximum magnetic field is 21.20 mT, and due to the absence of a magnetic core, there is no magnetic saturation.

B. Impedance Measurement

To verify the calculations in Figs. 9 and 11, the open-circuit impedance, short-circuit impedance, and common-mode impedance are measured at $T = 26$ °C using an impedance analyzer Wayne Kerr 6500B. Fig. 19(a) illustrates the measured results of the open-circuit input impedance Z_{OC} and short-circuit input impedance Z_{SC}. The resonance points are all greater than 6.85 MHz indicating that the parallel stray capacitance does not affect the circuit. Fig. 19(b) shows the common-mode impedance Z_{CM}, where the common-mode capacitance is 71.3 pF, and it has a strong ability to suppress common-mode interference.

Table III gives the error between the calculated, simulated, and measured inductance and resistance at $f_s = 200$ kHz and $T = 26$ °C. Compared with simulated and measured results, the calculated inductance error is within 10% and 5%, and the resistance error is less than 3% and 25%, respectively. In fact, due to the twisting of the Litz wire, when the calculated value is multiplied by the twisting factor 1.28 [26], its error with the measured value is within 5%. This also proves the accuracy of the proposed model. In addition, a low mutual resistance demonstrates that it is feasible to ignore it.

C. System-Level Experimental Waveforms

As shown in Figs. 20 and 21, the experimental waveforms at thermal steady state are tested for $P_o = 100\%P_r$ and $P_o = 50\%P_r$, respectively. The prototype adopts closed-loop self-sustained phase-shift control [39], and the output voltage is stabilized at 110 V. A gate drive voltage of +15/–4 V is employed to improve turn-off speed and noise immunity.

Fig. 20(a) shows the steady-state waveforms of v_{ab}, i_{Lp}, V_o, and i_{Ls} at $P_o = 1500$ W. The prototype outputs rated power, with almost zero phase shift angle, and the resonant waveforms are all sinusoidal. It can be seen that i_{Lp} is almost in phase with v_{ab} and differs from i_{Ls} by 160°. Fig. 20(b) shows the steady-state waveforms at $P_o = 750$ W. The self-sustained phase-shift control can simultaneously change the duty cycle and frequency to regulate the output voltage. From $P_o = 100\%P_r$ to $P_o = 50\%P_r$, the operating frequency also decreases from 192 to 184 kHz, and the ac resistance becomes smaller, but the duty cycle increases leading to an increase in reactive power circulating current.

Fig. 21(a) and (b) give the soft-switching waveforms at $P_o = 100\%P_r$ and $P_o = 50\%P_r$, respectively. The leading phase is

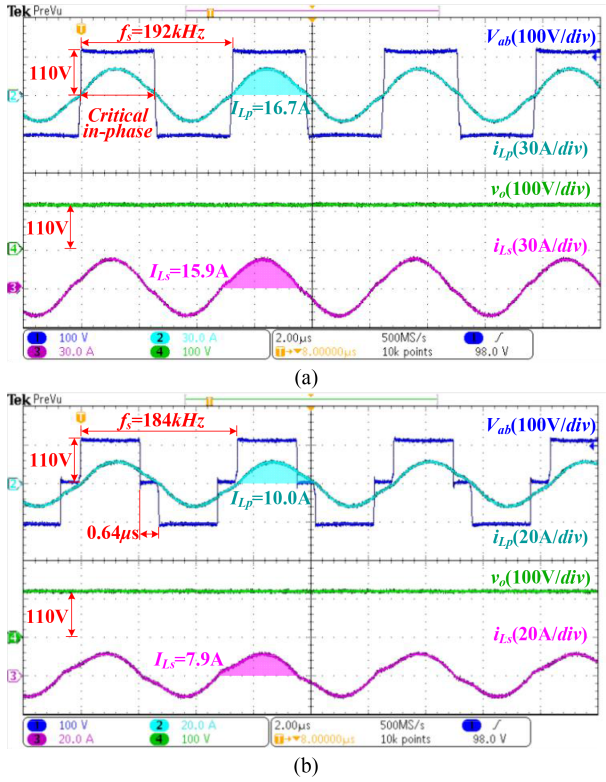

Fig. 20. Experimental waveforms of the prototype. (a) $P_o = 100\%P_r$ and $f_s =$ 192k Hz. (b) $P_o = 50\%P_r$ and $f_s = 184$ kHz.

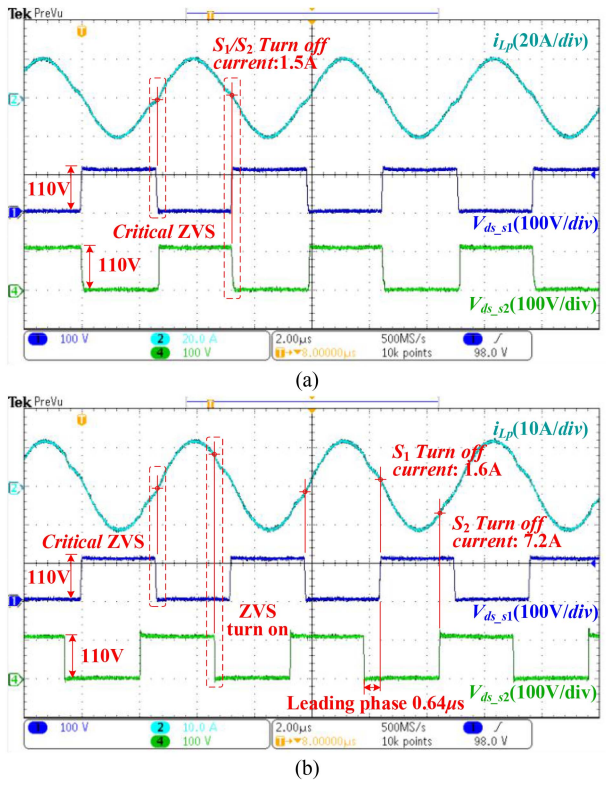

Fig. 21. Soft-switching waveforms of the prototype. (a) $P_o = 100\%P_r$. (b) $P_o = 50\%P_r$.

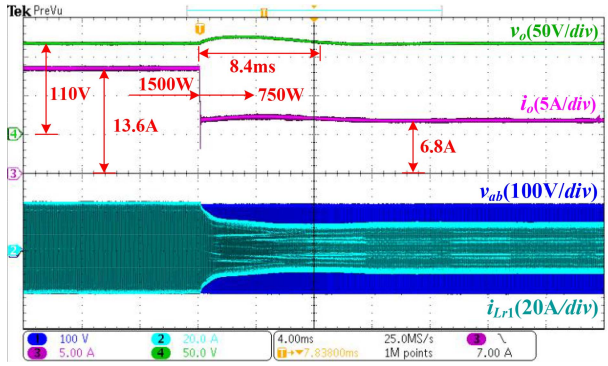

Fig. 22. Experimental dynamic waveforms form $P_o = 100\%P_r$ to $P_o = 50\%P_r$.

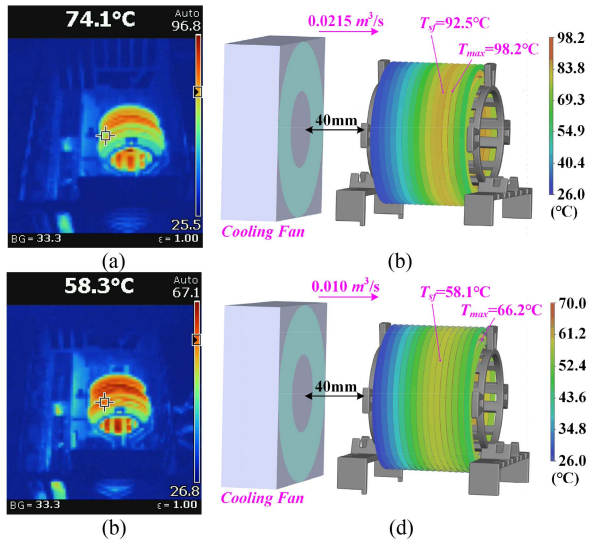

Fig. 23. Thermal images of prototype. (a) and (b) are measured and simulated thermal image at $P_o = 100\%P_r$. (c) and (d) are measured and simulated thermal image at $P_o = 50\%P_r$.

pre-set and all MOSFETs achieve the critical ZVS, eliminating the turn-ON loss. In Fig. 21(a), a near unity power factor is achieved, greatly reducing the RMS current and turn-OFF current (only 1.5 A) at the primary side. Fig. 21(b) gives the half-load soft-switching waveforms with leading phase 0.64 μs. The turn-OFF current of S_3 and S_4 in the lagging leg is 7.2 A, but that of S_1 and S_2 in the leading leg is only 1.6 A.

Fig. 22 illustrates the dynamic waveforms of v_o, i_o, v_{ab}, and i_{Lp} at the thermal steady state. When the output power is switched from $100\%P_r$ to $50\%P_r$, the output voltage is stabilized at 110 V after 8.4 ms with low overshoot.

D. System-Level Thermal and Efficiency Tests

To verify the thermal reliability of the prototype, the temperature rise test is verified at $P_o = 100\%P_r$ and $P_o = 50\%P_r$, with an ambient temperature of 26 °C.

Fig. 23(a) and (b) shows the experimental and finite element simulated thermal images of the CLT at $P_o = 100\%P_r$.

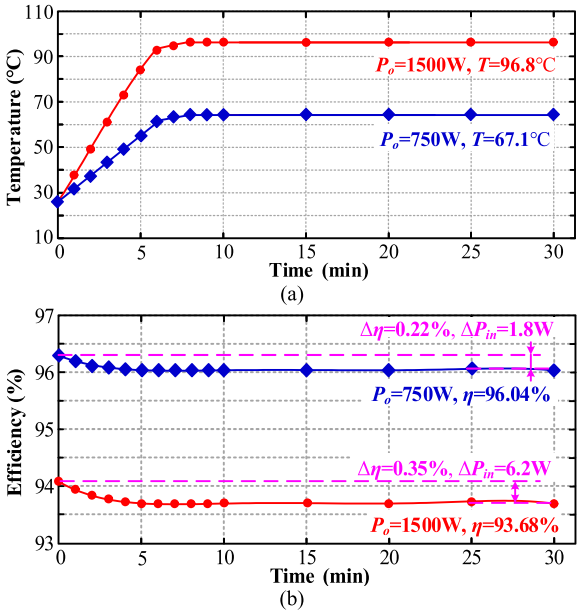

Fig. 24. Time versus temperature and input power curves. (a) Temperature-time curve. (b) Time-efficiency curve.

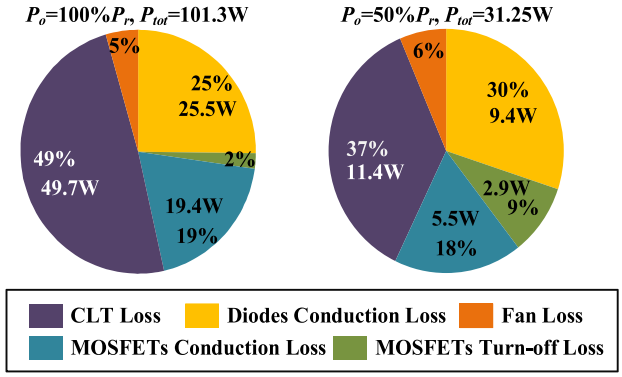

Fig. 25. Calculated loss distribution of prototype at $P_o = 100\%P_r$ and $P_o = 50\%P_r$.

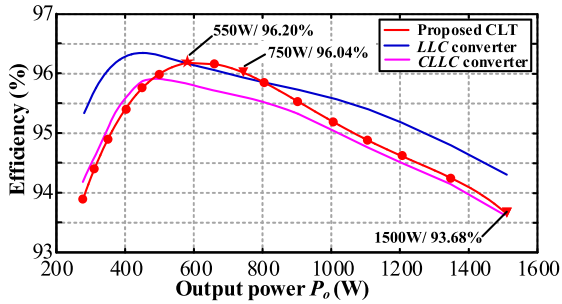

Fig. 26. Measured efficiency curve for system level at different output power.

The cooling fan has a power of 4.5 W and an air volume of 0.0215 m^3/s. The measured and simulated hotspots of the CLT are 96.8 and 98.2 °C, respectively, which are both lower than 110 °C. From the simulation, the surface temperature of the CLT is highest in the middle, which is similar to the practice. Since the hotspot in the inner layer is difficult to measure, the surface temperature rise is used as a reference. The simulated surface temperature, $T_{sf} = 92.5$ °C, is similar to the calculated 87.3 °C. The margin of 14 °C allows it to operate at a maximum ambient temperature of 40 °C. The heat sinks of semiconductors have a low temperature of 32.2 °C.

Fig. 23(c) and (d) shows the comparison of experimental and simulated thermal images at $P_o = 50\%P_r$. The cooling fan has a power of 2 W and an air volume of 0.010 m^3/s. Due to lower loss, its measured surface hotspot is only 67.1 °C, which is similar to the simulated hotspot of $T_{sf} = 58.1$ °C.

The temperature–time curve is given in Fig. 24(a). The thermal steady state is established within 10 min at $P_o = 100\%P_r$ and $P_o = 50\%P_r$. Fig. 24(b) shows the time-efficiency curve during the heat runs. The change of input power with temperature is not significant, i.e., the efficiency is not significantly affected by temperature, which is attributed to the increase in skin depth and the lower average ΔT of the CLT.

According to (21) and (26)–(29), the loss distribution of the prototype at $P_o = 100\%P_r$ and $P_o = 50\%P_r$ can be calculated as shown in Fig. 25. The loss of resonant capacitors is too small to be ignored. At $P_o = 100\%P_r$, the calculated loss and conversion efficiency of the prototype are 101.30 W and 93.69%, respectively. Its main losses come from the CLT and diodes, which account for 49.7% and 25.5%, respectively. This is consistent with the thermal distribution shown in Fig. 23(a). At $P_o = 50\%P_r$, the calculated efficiency of the prototype reaches 96.0%. The calculated loss of the CLT is only 11.4W, with a conversion efficiency of 98.5%. The reason is that the AC resistance and temperature rise of CLT are smaller at $P_o = 50\%P_r$. To improve the efficiency of the prototype, more strands of Litz wire can be selected.

Fig. 26 gives the system-level measured efficiency curve of the prototype at different output power, and the data is taken at the thermal steady state. At $P_o = 100\%P_r$ and $P_o = 50\%P_r$, the measured efficiencies are 93.68% and 96.04%, respectively. The calculated errors are all within acceptable limits. The peak efficiency is 96.20% at $P_o = 550$ W. Under light load conditions, the increase in the duty cycle leads to an increase in reactive power circulating current, and the conversion efficiency becomes low. It is worth noting that the proposed *CLLC* CLT can achieve conversion efficiency similar to conventional *LLC* and *CLLC* converters.

VII. Comparison and Expansion of Technologies

A. Comparison of Technologies

As shown in Table IV, the proposed CLT is compared with the magnetic devices of the *LLC* and *CLLC* converters designed using the AP method [17]. The results are as follows.

1) The winding of the CLT is directly air-cooled, so the larger J_c is designed to produce a VPD similar to that of the magnetic devices of the *LLC* and *CLLC* converters.
2) By multiplexing the leakage inductance and without a magnetic core, the GPD of the proposed CLT is almost

TABLE IV
COMPARISON OF TECHNOLOGIES

Parameters	Proposed CLT	Magnetic Devices of the *LLC* and *CLLC* converters
Design specifications (Note: *LLC* converter does not include L_{r2})		
$L_{r1}/L_m/L_{r2}$ (μH)	7.4/17.8/7.4	7.4/85.1/7.8
$N_{Lr1}/N_T/N_{Lr2}$ (*turn*)	-/24:26	10/8:9/10
$l_{Lr1}/l_T/l_{Lr2}$ (*m*)	-/4:4.34/-	0.76/1.2:1.6/0.78
Wire weight (g)	170.0	44.0/77.2/47.0
Core	-	L_{r1}/L_{r2}:EE40 (50.1g) *T*:EE50 (112.2g)
J_c (A/mm^2)	8.3	5.2
Litz wire (d_z=0.05mm)	1000	1500
f_s (Hz)	128k~189k	200k
Power density		
GPD (W/g)	8.57	*LLC/CLLC*: 5.29/3.94
VPD (W/cm^3)	13.06	*LLC/CLLC*: 13.30/10.04
Efficiency & Loss at P_o=100%P_r		
Cal. Core Loss (W)	-	EE40/EE50: 5.89/13.14
Cal. Copper loss (W)	49.7W	EE40/EE50: 4.46/15.68
Cal. Eff. of device	96.79%	*LLC/CLLC*: 97.46%/96.80%
Meas. Eff. of system	93.68%	*LLC/CLLC*: 94.31%/93.62%

twice that of the magnetic devices for the *CLLC* converter with the same circuit structure.

3) The proposed CLT achieves conversion efficiency and dimensions similar to that of magnetic devices.

Compared with 3.61 W/g and 6.1 W/cm^3 of the CLT in [26], the proposed methodology significantly optimizes the power density, which can reach 8.57 W/g and 13.06 W/cm^3. Besides, the modular unit solution saves manufacturing costs and increases productivity.

B. Extended Application for 1:N Voltage Ratio

In the article, only CLTs with 1:1 voltage ratios suitable for dc bus-tie applications are considered. Therefore, it is necessary to point out that the proposed design methodology is still utilized for more 1:*N* voltage ratio applications. Simply set the axial layers to N_{pym} and N_{sym} for the primary and secondary units shown in Fig. 8, respectively. Furthermore, it can be extended for the design of CLTs for other circuits such as the phase-shifted full-bridge converter and the series resonant converter, etc.

VIII. CONCLUSION

This article presents the design of axial winding segmented coreless transformers based on analytical models of circuit, inductance, ac resistance, thermal, and system loss for fine design of electrical, structural, and thermal parameters. The electrical parameters of 1:1 self-sustained CLTs are optimized to reduce the consumption of Litz wires when the inductance ratio is 2.414. Then, the correction factor is introduced to modify the ac resistance calculation of the multilayer CLT, so that the error with the simulation is only within 3%. Furthermore, the loss-thermal iterative model and system loss model are developed to predict the temperature rise and compensate for the loss of output voltage. A uniformly sized prototype is established. It has an efficiency of 93.68% at 1500 W, with a peak efficiency of 96.20% at 550 W. The proposed model is compared with simulation and practice, inductance error is within acceptable 10% and 5%, and ac resistance error is within acceptable 3% and 25% respectively. Overall, the proposed methodology optimizes the cost and dimensions utilizing the axial winding multisegmented design, and the modular unit solution also increases productivity.

REFERENCES

[1] R. W. A. A. De Doncker, D. M. Divan, and M. H. Kheraluwala, "A three-phase soft-switched high-power-density DC/DC converter for high-power applications," *IEEE Trans. Ind. Appl.*, vol. 27, no. 1, pp. 63–73, Jan./Feb. 1991.

[2] B. Zhao, Q. Song, W. Liu, and Y. Sun, "Overview of dual-activebridge isolated bidirectional DC–DC converter for high-frequency-link power-conversion system," *IEEE Trans. Power Electron.*, vol. 29, no. 8, pp. 4091–4106, Aug. 2014.

[3] A. Nami, J. Liang, F. Dijkhuizen, and G. D. Demetriades, "Modular multilevel converters for HVDC applications: Review on converter cells and functionalities," *IEEE Trans. Power Electron.*, vol. 30, no. 1, pp. 18–36, Jan. 2015.

[4] S. Falcones, R. Ayyanar, and X. Mao, "A DC–DC multiport-converter-based solid-state transformer integrating distributed generation and storage," *IEEE Trans. Power Electron.*, vol. 28, no. 5, pp. 2192–2203, May 2013.

[5] Z. Tong, W. D. Braun, and J. M. Rivas-Davila, "Design and fabrication of three-dimensional printed air-core transformers for high-frequency power applications," *IEEE Trans. Power Electron.*, vol. 35, no. 8, pp. 8472–8489, Aug. 2020.

[6] T. Sen, Y. Elasser, and M. Chen, "Origami inductor: Foldable 3-D polyhedron multiphase air-coupled inductors with flux cancellation and faster transient," *IEEE Trans. Power Electron.*, vol. 39, no. 6, pp. 7312–7328, Jun. 2024.

[7] S. Yin et al., "A 1-MHz GaN-based *LCLC* resonant step-up converter with air-core transformer for satellite electric propulsion application," *IEEE Trans. Ind. Electron.*, vol. 69, no. 11, pp. 11035–11045, Nov. 2022.

[8] J. X. Jin et al., "HTS power devices and systems: Principles characteristics performance and efficiency," *IEEE Trans. Appl. Supercond.*, vol. 26, no. 7, Oct. 2016, Art. no. 3800526.

[9] X. Wang et al., "Normal zone initiation and propagation in Y-Ba-Cu-O coated conductors with Cu stabilizer," *IEEE Trans. Appl. Supercond.*, vol. 15, no. 2, pp. 2586–2589, Jun. 2005.

[10] H. Song and J. Schwartz, " Stability and quench behavior of YBa2Cu 3O7−x coated conductor at 4.2 K self-field," *IEEE Trans. Appl. Supercond.*, vol. 19, no. 5, pp. 3735–3743, Oct. 2009.

[11] O. C. Spro, F. Mauseth, and D. Peftitsis, "High-voltage insulation design of coreless, planar PCB transformers for multi-MHz power supplies," *IEEE Trans. Power Electron.*, vol. 36, no. 8, pp. 8658–8671, Aug. 2021.

[12] Z. Zhang, K. Xu, Z.-W. Xu, J. Xu, X. Ren, and Q. Chen, "GaN VHF converters with integrated air-core transformers," *IEEE Trans. Power Electron.*, vol. 34, no. 4, pp. 3504–3515, Apr. 2019.

[13] J. Serrano, I. Lope, J. Acero, J. M. Burdío, C. Carretero, and R. Alonso, "Design and optimization of small inductors on extra-thin PCB for flexible cooking surfaces," in *Proc. IEEE Appl. Power Electron. Conf. Expo.*, 2015, pp. 177–182.

[14] P. Czyz, T. Guillod, F. Krismer, J. Huber, and J. W. Kolar, "Design and experimental analysis of 166 kW medium-voltage medium-frequency air-core transformer for 1:1-DCX applications," *IEEE J. Emerg. Sel. Topics Power Electron.*, vol. 10, no. 4, pp. 3541–3560, Aug. 2022.

[15] P. Czyz et al., "Analysis of the performance limits of 166 kW/7 kV air- and magnetic-core medium-voltage medium-frequency transformers for 1:1-DCX applications," *IEEE J. Emerg. Sel. Topics Power Electron.*, vol. 10, no. 3, pp. 2989–3012, Jun. 2022.

[16] T. Guillod, P. Czyz, and J. W. Kolar, "Geometrical optimization of medium-frequency air-core transformers for DCX applications," *IEEE J. Emerg. Sel. Topics Power Electron.*, vol. 10, no. 4, pp. 4319–4335, Aug. 2022.

[17] W. G. Hurley, *Transformers and Inductors for Power Electronics: Theory, Design and Applications*. Hoboken, NJ, USA: Wiley, 2013, pp. 94–98.

[18] W. T. McLyman, *Transformer and Inductor Design Handbook*. Berlin, Germany: Springer, 2013, pp. 162–164.

[19] A. Garcia-Bediaga, I. Villar, A. Rujas, L. Mir, and A. Rufer, "Multiobjective optimization of medium-frequency transformers for isolated soft-switching converters using a genetic algorithm," *IEEE Trans. Power Electron.*, vol. 32, no. 4, pp. 2995–3006, Apr. 2017.

[20] C. Marxgut, J. Muhlethaler, F. Krismer, and J. W. Kolar, "Multiobjective optimization of ultraflat magnetic components with PCB-integrated core," *IEEE Trans. Power Electron.*, vol. 28, no. 7, pp. 3591–3602, Jul. 2013.
[21] Z. Wang, C. L. Bak, H. Wang, H. Sørensen, and F. F. da Silva, "Multiphysics digital model of the high frequency transformer for power electronics application considering electro-thermal interactions," *IEEE Trans. Power Electron.*, vol. 38, no. 11, pp. 14345–14359, Nov. 2023.
[22] T. O. Olowu, H. Jafari, M. Moghaddami, and A. I. Sarwat, "Multiphysics and multiobjective design optimization of high-frequency transformers for solid-state transformer applications," *IEEE Trans. Ind. Appl.*, vol. 57, no. 1, pp. 1014–1023, Jan./Feb. 2021.
[23] R. Bosshard and J. W. Kolar, "Multi-objective optimization of 50 kW/85 kHz IPT system for public transport," *IEEE J. Emerg. Sel. Topics Power. Electron.*, vol. 4, no. 4, pp. 1370–1382, Dec. 2016.
[24] B. Chen, X. Liang, and N. Wan, "Design methodology for inductor-integrated Litz-wired high-power medium-frequency transformer with the nanocrystalline core material for isolated DC-link stage of solid-state transformer," *IEEE Trans. Power Electron.*, vol. 35, no. 11, pp. 11557–11573, Nov. 2020.
[25] G. K. Y. Ho, Y. Fang, and B. M. H. Pong, "A multiphysics design and optimization method for air-core planar transformers in high-frequency *LLC* resonant converters," *IEEE Trans. Ind. Electron.*, vol. 67, no. 2, pp. 1605–1614, Feb. 2020.
[26] L. Lai, B. Zhang, and J. Lin, "PT-symmetric *CLLC* coreless transformer with magnetic potential balance," *IEEE Trans. Ind. Electron.*, vol. 71, no. 10, pp. 12436–12446, Oct. 2024.
[27] J. Reinert, A. Brockmeyer, and R. W. A. A. De Doncker, "Calculation of losses in ferro- and ferrimagnetic materials based on the modified Steinmetz equation," *IEEE Trans. Ind. Appl.*, vol. 37, no. 4, pp. 1055–1061, Jul./Aug. 2001.
[28] P. L. Dowell, "Effects of eddy currents in transformer windings," *Proc. Inst. Elect. Eng.*, vol. 113, no. 8, pp. 1387–1394, Aug. 1966.
[29] Z. Liu, J. Zhu, and L. Zhu, "Accurate calculation of eddy current loss in Litz-wired high-frequency transformer windings," *IEEE Trans. Magn.*, vol. 54, no. 11, Nov. 2018, Art. no. 8401605.
[30] C. Feeney, J. Zhang, and M. Duffy, "AC winding loss of phase-shifted coupled windings," *IEEE Trans. Power Electron.*, vol. 31, no. 2, pp. 1472–1478, Feb. 2016.
[31] M. Lu and K. D. T. Ngo, "Analytical calculation of proximity-effect resistance for planar coil with Litz wire and ferrite plate in inductive power transfer," *IEEE Trans. Ind. Appl.*, vol. 55, no. 3, pp. 2984–2991, May/Jun. 2019.
[32] J. Acero, R. Alonso, J. M. Burdio, L. A. Barragan, and D. Puyal, "Frequency-dependent resistance in Litz-wire planar windings for domestic induction heating appliances," *IEEE Trans. Power Electron.*, vol. 21, no. 4, pp. 856–866, Jul. 2006.
[33] J. Acero, R. Alonso, L. A. Barragan, and J. M. Burdio, "Magnetic vector potential based model for eddy-current loss calculation in round-wire planar windings," *IEEE Trans. Magn.*, vol. 42, no. 9, pp. 2152–2158, Sep. 2006.
[34] M. Jaritz, L. A. Barragan, and J. M. Burdio, "General analytical model for the thermal resistance of windings made of solid or Litz wire," *IEEE Trans. Power Electron.*, vol. 34, no. 1, pp. 668–684, Jan. 2019.
[35] J. Biela and J. W. Kolar, "Cooling concepts for high power density magnetic devices," in *Proc. Power Convers. Conf.*, 2007, pp. 1–8.
[36] A. van den Bossche et al., *Inductors and Transformers for Power Electronics*. Boca Raton, FL, USA: CRC Press, 2005, pp. 288–308.
[37] C. Jiang et al., "A hybrid compensation method for ICT high voltage power supply," *IEEE Trans. Appl. Supercond.*, vol. 30, no. 4, Jun. 2020, Art. no. 0600105.
[38] D. Hu et al., "A numerical method for calculating and optimizing the coupling factor of HTS air-core transformer," *IEEE Trans. Appl. Supercond.*, vol. 26, no. 6, Sep. 2016, Art. no. 5501106.
[39] H. Pinheiro, P. K. Jain, and G. Joos, "Self-sustained oscillating resonant converters operating above the resonant frequency," *IEEE Trans. Power Electron.*, vol. 14, no. 5, pp. 803–815, Sep. 1999.

Li Lai received the B.Eng. and the M.Sc. degrees in electrical engineering from East China Jiaotong University, Nanchang, China, in 2018 and 2021, respectively. He is currently working toward the Ph.D. degree with the School of Electric Power, South China University of Technology, Guangzhou, China.

In 2021, he was with CRRC ZIC Research Institute of Electrical Technology & Material Engineering, China, working on the development of high power conversion technology. His research interests include power converter, IGBT driver and application, and coreless isolation technology.

Bo Zhang (Fellow, IEEE) was born in Shanghai, China, in 1962. He received the B.S. degree in electrical engineering from Zhejiang University, Hangzhou, China, in 1982, the M.S. degree in power electronics from Southwest Jiaotong University, Chengdu, China, in 1988, and the Ph.D. degree in power electronics from the Nanjing University of Aeronautics and Astronautics, Nanjing, China, in 1994.

He is currently a Professor with the School of Electric Power, South China University of Technology, Guangzhou, China. He has authored or coauthored more than 600 papers and held more than 230 patents. He has authored nine monographs. His research interests include nonlinear analysis and control of power electronics, wireless power transfer technology, and ac drives.

Jingyang Lin was born in Fujian, China, in 1999. He received the B.S. degree in electronic science and technology from Northeastern University, Shenyang, China, in 2021. He is currently working toward the Ph.D. degree in power electronics with the School of Electric Power Engineering, South China University of Technology, Guangzhou, China.

His research interests include coreless isolation technology and power electronic converters.